Langmuir

Article

pubs.acs.org/Langmuir

Stationary Chemical Gradients for Concentration Gradient-Based Separation and Focusing in Nanofluidic Channels

Wei-Lun Hsu,[†] David W. Inglis,[‡,§] Helen Jeong,[‡] David E. Dunstan,[†] Malcolm R. Davidson,[†] Ewa M. Goldys,[§] and Dalton J. E. Harvie*[,†]

[†]Department of Chemical and Biomolecular Engineering, University of Melbourne, Victoria 3010, Australia

[‡]Department of Engineering and [§]MQ BioFocus Research Centre, Macquarie University, New South Wales 2109, Australia

Supporting Information

ABSTRACT: Previous work has demonstrated the simultaneous concentration and separation of proteins via a stable ion concentration gradient established within a nanochannel (Inglis et al. *Angew. Chem., Int. Ed.* **2001**, *50*, 7546−7550). To gain a better understanding of how this novel technique works, we here examine experimentally and numerically how the underlying electric potential controlled ion concentration gradients can be formed and controlled. Four nanochannel geometries are considered. Measured fluorescence profiles, a direct indicator of ion concentrations within the Tris−fluorescein buffer solution, closely match depth-averaged fluorescence profiles calculated from the simulations. The simulations include multiple reacting species within the fluid bulk and surface wall charge regulation whereby the deprotonation of silica-bound silanol groups is governed by the local pH. The three-dimensional system is simulated in two dimensions by averaging the governing equations across the (varying) nanochannel width, allowing accurate numerical results to be generated for the computationally challenging high aspect ratio nanochannel geometries. An electrokinetic circuit analysis is incorporated to directly relate the potential drop across the (simulated) nanochannel to that applied across the experimental chip device (which includes serially connected microchannels). The merit of the thick double layer, potential-controlled concentration gradient as a particle focusing and separation tool is discussed, linking this work to the previously presented protein trapping experiments. We explain why stable traps are formed when the flow is in the opposite direction to the concentration gradient, allowing particle separation near the low concentration end of the nanochannel. We predict that tapered, rather than straight nanochannels are better at separating particles of different electrophoretic mobilities.

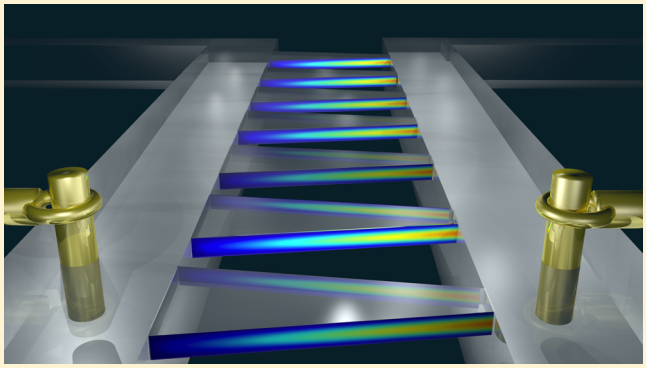

1. INTRODUCTION

Chemical gradients are ubiquitous. They help direct cell movement in biosystems, demonstrated to be important for bacteria survival.[1] In neutral systems, chemoattraction/chemorepulsion of cells in response to chemical gradients is a guidance mechanism in signal transduction and nerve growth in both in vitro and in vivo environments.[2] In semiconductor manufacturing, the manipulation of crystallizing ion concentration gradients near a substrate surface is used to fabricate advanced inorganic materials.[3] In analytical chemistry, stationary chemical gradients are the basis of a new class of separation devices. A chemical gradient stabilized within a micro/nanofluidic device has been used to produce very rapid preconcentration of proteins in physiological buffers,[4] representing a promising alternative to matrix-based methods such as isoelectric focusing and chromatographic gradient electrophoresis.[5,6] Recently, Inglis et al.[7] used a stationary ion gradient to simultaneously concentrate and separate proteins in a nanochannel. Chemical gradients have also been used to increase the sensitivity of immunosensors,[8] for amplified sample stacking,[9] for continuous-flow concentration polarization,[10] and for other particle separations.[5] The basis of these separation methods is that a localized accumulation or depletion of salt ions causes a perturbation in the conductivity and electric field and a flow, electroosmotic or other, carries the molecules to the perturbation site where they become trapped by opposing electrophoretic and viscous drag forces. For the effective design of these separation devices, the behavior of the underlying chemical gradient must be understood.

Controlled chemical gradients can be generated within micro/nanofluidic devices by a variety of means. Greenlee and Ivory[11] inserted a membrane between two flowing high and low salt concentration solutions (oriented parallel to the flow direction) to establish a concentration gradient within the high salt concentration channel. In a similar vein, Abhyankar et al.[12] used a high fluidic resistance membrane to create a

Received: January 23, 2014
Revised: April 11, 2014
Published: April 11, 2014

   dx.doi.org/10.1021/la500206b | *Langmuir* 2014, 30, 5337−5348

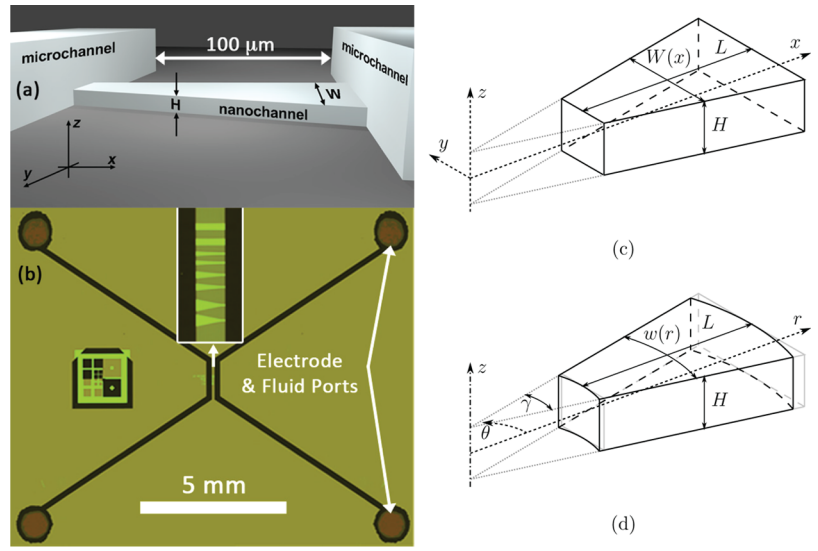

Figure 1. (a) Schematic of the nanochannel geometry and (b) layout of the microfluidic chip. Representation of the nanochannel in (c) Cartesian and (d) cylindrical coordinates. For illustration purposes, the height of the channel H has been greatly exaggerated in all images.

concentration gradient in a solution without fluid flow. Using gas absorption, de Jong et al.[13] employed a membrane separating liquid and gas phases within a microfluidic device to create a pH gradient. Irimia et al.[14] demonstrated that parallel dividers can be used to hinder the cross-stream diffusion of components flowing along a microfluidic channel, thus controlling a concentration gradient. While other methods such as concentration polarization[10] have also been used, the most popular method reported in the literature for producing a controlled chemical gradient within a micro/nanofluidic device involves connecting two reservoirs containing solutions of different concentrations by a channel.[15] The low Reynolds number laminar flow within these devices makes the developed gradients stable and easy to control. Jeon et al.[16] designed a concentration gradient generator using such a device and measured the fluorescence of fluorescein isothiocynate (FITC) concentrations in the absence of any applied electric field.

While the generation of stable concentration gradients within microchannels is reasonably well understood, stable gradient generation within nanochannels has received less attention. In nanofluidic devices, the double layer thickness is comparable to the channel depth, implying that ion concentrations are nonuniform across the entire channel depth. This *may* be advantageous in terms of particle trapping, but it also increases the complexity of modeling ion fluxes, fluid velocities, and bulk solution chemistry. Hence, in order to effectively validate the modeling of ionic gradients in nanochannels, a method is required to quantitatively visualize the locally varying solution chemistry. For this purpose, fluorescent reporter molecules at low concentration have been added to stronger salt solutions to visualize concentration gradients; however, such added fluorophores may actually misrepresent the gradients as they themselves may focus and hence not represent the concentration of the more dominant salt ions.[5] To the best of our knowledge, the direct visualization of salt/conductivity perturbation in a micro-nano−microchannel system has only been reported by Zangle and co-workers.[17,18] This group (primarily) used Alexa Fluor dye (lithium cation), which is pH insensitive and completely soluble in aqueous solutions, to visualize concentration polarization propagation at microchannel and nanochannel junctions (they did present one result employing fluorescein but did not explore this fully due to its pH-dependent fluorescence in their unbuffered system). A one-dimensional, semiquantitative model was developed to explore under what conditions concentration polarization shocks formed and the velocity at which they travel.[19]

In terms of modeling gradient-based focusing, previous studies are also generally limited to systems that have a double layer thickness that is much smaller than the channel depth, that is, microfluidic systems. Petsev et al.[20] used a momentum balance that neglected viscous and pressure terms to calculate the movement of a solution under the action of an electric force and assumed that the average velocity equals the product of the bulk electroosmotic mobility and applied electric field strength. Ghosal and Horek[21] applied Helmholtz−Smoluchowski slip boundary conditions on wall surfaces to consider electroosmotic behavior under an axial electric field gradient in a microchannel. In nanofluidic devices, these modeling assumptions are inaccurate. Also, in the context of modeling concentration gradients, the previous theoretical studies[22−24] generally only consider binary ionic species (e.g., Na^+ and Cl^-) and neglect other secondary species such as H^+, OH^-, and buffer ions. However, if quantitative agreement with experiment is to be achieved, including these secondary species is necessary as the silica surface charge density is pH regulated by surface silanol groups.[25−27] In the context of detailed nanochannel simulations, results for multiple ionic species systems which comprise Na^+, Cl^-, H^+, and OH^- (for example) have recently been presented:[28,29] Weak acid and base buffered solutions (that are so relevant to biological applications) require further study however.

In this study, we demonstrate the generation and voltage-control of a stationary ion gradient within four different (straight and tapered) 75 nm deep nanochannel geometries. A Tris−fluorescein (TF) electrolyte is employed. As for the electrolyte chosen by Zangle and co-workers in their study of concentration polarization and shock propagation,[17,18] the concentration indicating ion (fluorescein) is a dominant ion in the TF electrolyte, meaning that measured fluorescence is a true indicator of the pertinent concentration gradient. Also, as the solution is buffered by Tris, the pH variation in regions where the fluorescein ions are present is significantly reduced,

dx.doi.org/10.1021/la500206b | *Langmuir* 2014, 30, 5337−5348

allowing the measured fluorescence to semiquantitatively represent depth-averaged anion concentrations. Detailed numerical simulations give further insight into the experimental system. The simulations are performed using two-dimensional, width-averaged equations, and consider multiple, reacting ionic species within the buffered solution (H^+, OH^-, Tris, Tris$-H^+$, HFl^-, and Fl^{2-}). The dissociation of silanol groups on the silica channel walls in response to local pH is modeled (i.e., charge regulated surfaces). By comparing calculated and measured fluorescence profiles, we are able to validate the simulations and hence use the simulations to probe quantities that are not directly measurable, for example, ion concentration profiles of all species within the nanochannels. Further, by investigating the electric and hydrodynamic drag forces on modeled target molecules, we examine the molecular trapping effectiveness of the nanochannel system as a function of applied voltage and nanochannel geometry, providing a better understanding of how the separation devices that are based on these concentration gradients[7] work.

2. EXPERIMENTAL SECTION

Silicon/pyrex devices shown in Figure 1 were fabricated using standard semiconductor techniques (described elsewhere[7]). Four channel shapes were used: one rectangular and three trapezoidal, each 100 μm long. All solutions were diluted to the working concentration and filtered to 0.2 μm before placing in the device. Flow in each channel was between 20 and 150 nL/min. Each fluorescein molecule was buffered with two Tris molecules giving a bulk pH of 7.1 (measured). The microchannels on the right and left sides of the nanochannel carried TF solutions at 2000 and 6 μM, respectively. A biased voltage ($-1.5\sim1.5$ V) was applied between the two pairs of microchannel electrodes to generate the potential difference across the nanochannels. The ion gradients took only a few seconds to form and were stable.

To calibrate the measured fluorescence intensity to fluorescein ion concentrations, we pressure filled the nanochannels with 0.5 mM TF (333 μM Tris, 167 μM fluorescein) containing 0–300 mM NaCl. Below 50 mM NaCl, the intensity dropped with decreasing salt concentration, while above this, the intensity changed little with increasing salt concentration. This means that, above 50 mM NaCl, the double layers were thin so that the depth-averaged fluorescein concentration was equal to the bulk concentration. By using the model outlined in Section 3.2, at the calibration pH of 7.1, the relative fluorescence of the solution is 85.5% of the fluorescence that would be emitted if all of the fluorescein present was in its dianionic form (Fl^{2-}). Knowing this relative fluorescence allowed us to use the calibration test to express all measured fluorescence intensities as *intensity-interpreted dianionic fluorescein concentrations* that we define to be the depth-averaged concentration of (only) Fl^{2-} that would produce the measured fluorescence intensity. In line with the model discussed in Section 3.2, at high pH, this intensity-interpreted dianionic fluorescein concentration equals the actual depth-averaged fluorescein concentration. Beer–Lambert absorption at the fluorescein concentrations and channel depths is negligible.

3. THEORY

We predict the behavior of the ions within the nanochannels using numerical simulations. We use steady-state versions of the governing equations that represent the laminar flow of an incompressible Newtonian reacting electrolyte, namely, the continuity equation, Navier–Stokes equation (including an electrostatic term), the electric Poisson equation, and Nernst–Planck ion transport equations (including chemical reaction source terms).

3.1. Averaging the Governing Equations. Accurately solving this system of equations in three dimensions is computationally challenging due to the high aspect ratio (width to height) of the nanochannels. To calculate current/voltage curves for KCl solutions flowing through conical nanopores, Cervera et al.[30] averaged Nernst–Planck and Poisson equations over the cross section of the pores by assuming that the radial ionic fluxes were negligible and by ignoring the electroosmotic flow. Hence, in their study, reported variables represent values averaged over spherical shells. In a similar vein, Mani et al.[19] used a Cartesian-based averaging method (in the channel depth direction) on the Nernst–Planck equations to derive a one-dimensional partial differential equation describing flow through their slowly varying micronano–microchannel system. They assumed that the velocity profile was composed of a parabolic pressure-driven profile and a potential-determined electroosmotic profile based on the Helmholtz–Smoluchowski equation. Diffusion was treated in a semiqualitative manner.

In this study, we also average the governing equations across the nanochannel width, but as this width is not slowly varying in the axial direction, we perform this averaging in cylindrical coordinates. Full details are given in the Supporting Information, SI 1. Figure 1c shows the geometry of the nanochannel in rectangular coordinates: It is a rectangular wedge, with side walls located at $y = \pm W/2$ tapering linearly inward toward an origin that is located outside of the flow domain. The nanochannel intersects with the microchannels at both ends of the wedge shape. The height of the channel, H, is uniform, and at all x locations, this height is significantly less than the width of the channel W (that is, $H \ll W$). Figure 1d shows the cylindrical wedge used to represent the nanochannel in the simulations. Variables and cylindrical versions of the governing equations are averaged over circumferential arcs of length w that span the channel width (that is, lines of constant r), resulting in a two-dimensional system. Not only does this reduce computational requirements, but the coordinate change is also advantageous as the circumferential averaging arcs intersect normally with the side walls, simplifying the side wall boundary condition treatment. Note that, as the final averaged variables and governing equations are only functions of the two cylindrical coordinates r and z, the results can be interpreted using a two-dimensional, Cartesian coordinate system.

Several geometrical and physical assumptions are required to justify the averaging process. The primary geometrical assumption required is that the channel height is small. Note that as $W(x)$ and $w(r)$ are related by the constant $\gamma/\tan(\gamma)$, at any $x = r$, this assumption can be expressed as

$$H \ll w \tag{1}$$

In this study, it is implied that, when order of magnitude comparisons, we are comparing only the magnitude of terms and not their signs. The symbols $\sim$, $\lesssim$, $\gtrsim$, $\ll$, and $\gg$ denote order of magnitude comparisons. The primary physical assumption is that the height of the channel is smaller than or of a comparable magnitude to the double layer thickness:

$$H \lesssim \delta \tag{2}$$

Combined with the small channel height assumption, it follows that the (local) double layer thickness δ is also much smaller than the width of the channel:

$$\delta \ll w \tag{3}$$

The above assumptions imply that the double layers from the top and bottom walls overlap, so that at all locations within the

dx.doi.org/10.1021/la500206b | Langmuir 2014, 30, 5337–5348

flow domain, the local net charge within the fluid is nonzero, and the local electrical field is significantly affected by the surface charge from at least one wall. This allows us to assume that, for the majority of the variables, average values are approximately equal to local values, except near the side walls (located at $\theta = \pm \gamma/2$) where conditions are most affected by the side wall double layers. If we further assume that the average and local values have similar orders within these side wall double layers (reasonable for most variables as every point within the flow domain is affected by at least one double layer) then this combined assumption becomes, for a generic scalar ϕ,

$$\frac{\phi'}{\bar{\phi}}\begin{cases}\sim 1 & \text{if} \quad \frac{\gamma}{2} - \gamma_\delta < |\theta| < \frac{\gamma}{2} \\ \ll 1 & \text{otherwise}\end{cases} \tag{4}$$

where $\gamma_\delta = \delta/r$ is the local angular double layer width. In the subsequent analysis, we assume that eq 4 applies to the two velocity components v_r and v_z (laminar flow assumed), the net fluid charge density ρ_e, the concentration of the ith species n_i, and the potential gradients $(\partial U)/(\partial r)$ and $(\partial U)/(\partial z)$, where U is the potential.

Finally, consistent with the assumption of flow occurring in predominantly the r-z plane, we assume

$$\frac{v_\theta}{\bar{v}_z} \lesssim 1 \quad \text{and} \quad \frac{v_\theta}{\bar{v}_r} \lesssim 1 \tag{5}$$

By utilizing these assumptions, the averaged governing equations can be expressed in two-dimensional Cartesian coordinates as follows (detailed in the Supporting Information, SI 2):

$$\frac{1}{W}\nabla\cdot W\boldsymbol{v} = 0 \tag{6}$$

$$\frac{\varepsilon\varepsilon_0}{W}\nabla\cdot W\nabla U = -\rho_e \tag{7}$$

$$\frac{\rho}{W}\nabla\cdot W\boldsymbol{vv} = -\nabla p + \frac{\mu}{W}\nabla\cdot W\nabla\boldsymbol{v} - \rho_e\nabla U \tag{8}$$

$$\frac{1}{W}\nabla\cdot W\boldsymbol{j}_i = S_i \tag{9}$$

$$\boldsymbol{j}_i = n_i\boldsymbol{v} - \mathcal{D}_i\left[\nabla n_i + \frac{z_i e}{k_B T}n_i\nabla U\right] \tag{10}$$

$$\rho_e = \sum_i z_i e n_i \tag{11}$$

where $W(x)$ is the local channel width, ρ is the fluid density, p is the pressure, ε is the dielectric constant, ε_0 is the permittivity of vacuum, μ is the viscosity, $\boldsymbol{v}$ is the velocity, k_B is the Boltzmann constant, T is the temperature, e is the electron charge, $\boldsymbol{j}_i$, S_i, z_i and $\mathcal{D}_i$ are the ionic flux, reaction term, signed valency and diffusivity of species i, respectively, and the sum in eq 11 is over all charged species present. Note that, for constant W (that is, a straight channel), these equations become notationally identical to their unaveraged Cartesian forms, implying that, given the assumptions employed in our analysis, the side wall double layers do not affect the width-averaged flow behavior within the nanochannels.

3.2. Chemical Reactions. In general, five dissociation reactions affect the local concentrations of the eight species in our TF system:

$$\mathrm{H_2O} \leftrightarrow \mathrm{H^+ + OH^-}$$

$$\mathrm{Tris{-}H^+ \leftrightarrow Tris + H^+}$$

$$\mathrm{HFl^- \leftrightarrow Fl^{2-} + H^+} \tag{12}$$

$$\mathrm{H_3Fl^+ \leftrightarrow H_2Fl + H^+}$$

$$\mathrm{H_2Fl \leftrightarrow HFl^- + H^+} \tag{13}$$

However, except under very acidic conditions (pH $\leq$ 4.5), fluorescein molecules (H_2Fl) generally release protons in aqueous solutions meaning that the monoanion and dianion forms (i.e., HFl^- and Fl^{2-}) are dominant and the cation and neutral forms (i.e., H_3Fl^+ and H_2Fl) can be neglected.[31] Hence, we simplify our model by neglecting the protonization and first deprotonization reactions of fluorescein and consider only the three dissociation reactions and six related species in eq 12 (this simplification is validated in the Supporting Information, SI 3).

The local forward rate of each reaction listed in eq 12 is given by

$$R_1 = k_w(K_w - n_{H^+}n_{OH^-}) \tag{14}$$

$$R_2 = k_{Tris}\left(K_{a,Tris} - \frac{n_{Tris}n_{H^+}}{n_{Tris-H^+}}\right) \tag{15}$$

$$R_3 = k_{fluorescein}\left(K_{a,fluorescein} - \frac{n_{Fl^2}n_{H^+}}{n_{HFl^-}}\right) \tag{16}$$

where k_w, k_{Tris}, and $k_{fluorescein}$ are the reaction constants for water dissociation, Tris protonation, and second fluorescein deprotonation, respectively, and K_w, $K_{a,Tris}$, and $k_{a,fluorescein}$ are the corresponding equilibrium constants. Reliable values for the Tris protonation and second fluorescein deprotonation reaction constants are not readily available. Hence, we use the water dissociation reaction value for these constants. Sensitivity tests have shown that, provided these two constants (k_{Tris} and $k_{fluorescein}$) are in the same range as that for water (k_w), the computational results are quite insensitive to their specific values. Finally, stoichiometry of eq 12 is used to express the local source terms S_i used in the Nernst–Planck equations (eq 9) in terms of the local reaction rates: $S_{H^+} = R_1 + R_2 + R_3$, $S_{OH^-} = R_1$, $S_{Tris} = R_2$, $S_{Tris-H^+} = -R_2$, $S_{HFl^-} = -R_3$, and $S_{Fl^{2-}} = R_3$.

The charge on the nanochannel surface depends upon the degree of dissociation and the number density of silanol groups it carries. This dissociation reaction can be described by

$$\mathrm{SiOH \leftrightarrow SiO^- + H^+} \quad \text{and} \quad K_{a,silanol} = \frac{[\equiv SiO^-]_s n_{H^+}}{[\equiv SiOH]_s} \tag{17}$$

where $[\equiv SiO^-]_s$ and $[\equiv SiOH]_s$ are the concentrations of silanol groups and silicic acid groups on the nanochannel surface, respectively, and $K_{a,silanol}$ is the silanol group equilibrium constant. Assuming local equilibrium, eq 17 leads to an expression for the surface charge in terms of the local H+ concentration as

$$\sigma_d = -e\Gamma\frac{K_{a,silanol}}{K_{a,silanol} + n_{H^+}} \tag{18}$$

where Γ is the number density of the silanol groups. Reaction parameters used in simulations are listed in Table 1.

dx.doi.org/10.1021/la500206b | Langmuir 2014, 30, 5337−5348

Table 1. Reaction Constants and Number Density of the Silanol Groups Used in the Simulations

variable	value	ref
$k_w = k_{Tris} = k_{fluorescein}$	1.4×10^{11} 1/(s M)	
pK_w	14	
$pK_{a,Tris}$	8.06	Persat et al.[32]
$pK_{a,fluorescein}$	6.36	Diehl and Markuszewski[31]
$pK_{a,silanol} = 7.5$	7.5	Andersen et al.[25] and Behrens and Grier[26]
Γ	5 nm^{-2}	Lorenz et al.[27]

3.3. Nanochannel Computational Method. Even with the use of the averaged governing equations, the widely varying length scales of the physical device present some numerical challenges. Two techniques are used to circumvent these difficulties. (a) As the microchannels that feed the nanochannels have a height that is orders of magnitude larger than the nanochannel height (10 μm vs 75 nm), the microchannels cannot be simulated in their entirety via the same two-dimensional simulations employed to model the nanochannel flows. Instead full two-dimensional simulations are performed only within individual nanochannels, with the affects of the microchannels on these simulations incorporated via an electrokinetic circuit analysis that is used to determine the appropriate boundary conditions (detailed in the next two sections). "Reservoir" regions having a relatively large height and width are added to the end of the nanochannel flow domain to model the interface between the two length scale geometries (see Figure 2). Conditions at the ends of the reservoirs represent those in the attached microchannels. (b) Second, as the length to height ratio of each nanochannel is large (greater than 1000), the simulation flow domain is discretized using a hybrid structured/unstructured mesh that is able to resolve the flow accurately while keeping computational costs within practical limits. Within the nanochannel themselves, a structured mesh is used with cell size varying in both the axial and cross-stream directions to concurrently resolve both the electric double layers and flows occurring around the nanochannel ends. Within the reservoirs, a combination of structured and unstructured cells is used to allow a smooth transition between the fine mesh elements of the nanochannel double layer/ends and coarse mesh elements at the reservoir ends. Symmetry along the channel half-plane is assumed to further decrease the computational cost: While this slightly misrepresents the shape of the connecting microchannel regions, testing showed that, provided the reservoirs are large enough, their actual shape has little effect on the results. Figure 2 provides more detail.

A careful mesh sensitivity analysis is conducted to ensure that the flow within the nanochannels was adequately resolved. Using the presented mesh structure, we are able to generate effectively mesh-independent results using approximately 134 000 computational cells. Details of boundary conditions applied in the simulations are available in the Supporting Information, SI 4.

The open-source multiphysics solver *arb*[33] is used to solve the system of equations and boundary conditions. *arb* discretises transport equations using an implicit finite-volume method and solves the resulting numerical system via a backstepped, Newton−Raphson method. In the context of electrokinetic and nano/microfluidic flows, this solver has been used to calculate the electrokinetic flow of a binary electrolyte

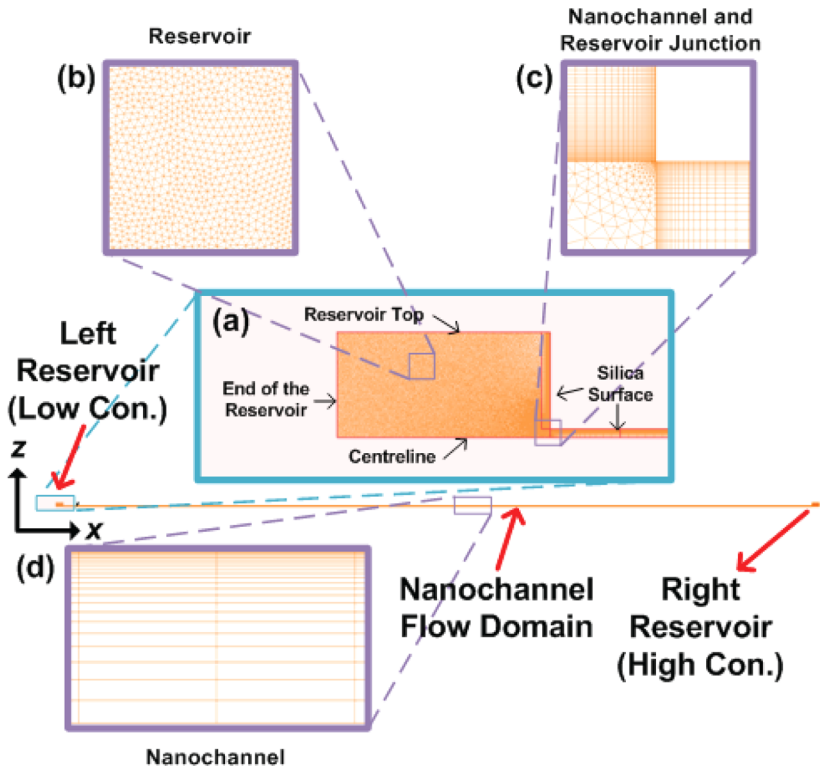

Figure 2. (a) Two-dimensional numerical simulations are performed within a flow domain composed of a single nanochannel sandwiched between two reservoirs. The reservoirs model the junction with the surrounding microchannels. Insets show example mesh detail within: (b) the body of the reservoirs, (c) the nanochannel and reservoir junction area, and (d) the nanochannel.

dx.doi.org/10.1021/la500206b | *Langmuir* 2014, 30, 5337−5348

through parallel nanochannels,[34] pressure and potential losses resulting from electrokinetic flow through nanofluidic bends and junctions,[35] and interfacial mass transfer and reaction in a Y−Y microfluidic channel.[36,37] Input files that demonstrate the discretization technique for the flow of a binary electrolyte through a charged channel are available for download.[38] The computational mesh was generated using the open-source program *gmsh*.[39]

3.4. Electrokinetic Circuit Analysis. As mentioned in Section 3.3, the large length scale difference in the device necessitates the use of a circuit analysis to capture the effects of the microchannels on the concentration gradients produced in the nanochannels.

A schematic of the network is shown in Figure 3. Fluid enters the network via the two circular ports on the right and leaves via the two ports on the left. Fluid in the upper microchannel is at a low potential and has a low electrolyte concentration. Fluid in the lower microchannel is at a high potential and has a high electrolyte concentration. Eight parallel nanochannels connect the upper and lower microchannels; only one of these nanochannels can be simulated at once using two-dimensional simulations. Our objective here is to relate the potential difference existing over the length of one of these nanochannels Δu (that is, to be applied in the simulations) to the potential difference applied between the ports (electrodes) of the microfluidic chip ΔU that contains all eight nanochannels (that is, those reported in the experiments).

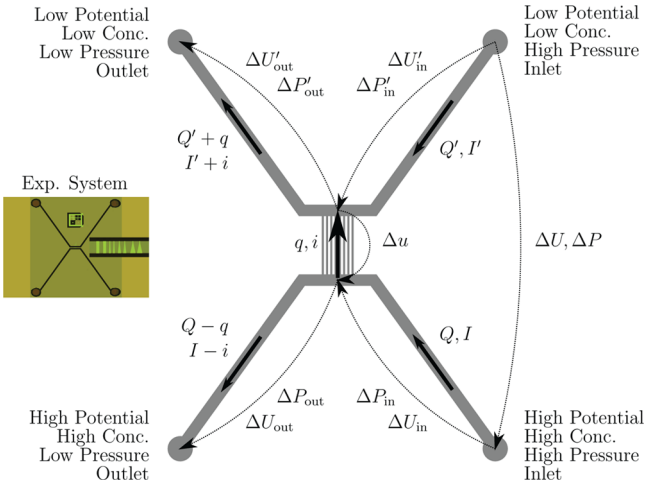

Figure 3. Schematic of the electrokinetic circuit contained on the chip.

The network analysis is based on conservation of fluid flow and conservation of total charge. This type of circuit model is referred to as a Total Current Model (TCM).[40] We note that, in general, conservation of ion currents (the current due to the flux of one ion species), rather than just the total current, is required in electrokinetic circuit analysis. However, in the present system, the double layers within the microchannels are small relative to the microchannel depth (10 μm), so on the basis of previous analysis of a similar system,[40,41] we expect the TCM to be adequate. This assumption is equivalent to assuming that the (geometric mean) ion concentration is the same in both of the inlet and outlet legs of the two microchannels. Note that numerical simulations are used to predict the ion current behavior within the nanochannels and so do not require this thin double layer assumption.

The flux variables q and i employed in the circuit analysis represent the total flow rate and current moving through all of the eight parallel nanochannels, whereas the simulations predict the flow rate q_{sim} and current i_{sim} that flows through a single straight nanochannel. As the eight parallel nanochannels are of different geometries, to quantitatively calculate the total fluxes from simulation results, we would need to simulate every nanochannel geometry for each applied voltage. For practical reasons, we have not done this. Instead, we assume that the

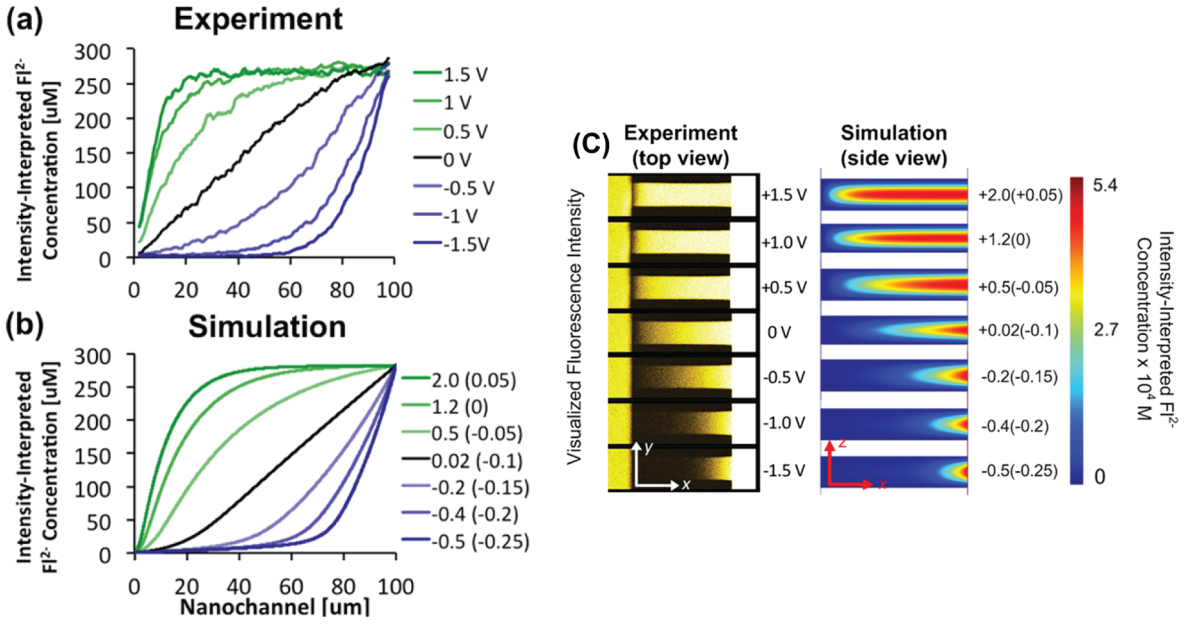

Figure 4. Concentrations within the rectangular nanochannel: (a) experimental and (b) theoretical average intensity-interpreted Fl^{2-} concentration in a rectangular nanochannel at various levels of applied voltages (outside braces: ΔU; inside braces: Δu). Frame (c) shows the top view (x−y plane) of the experimental fluorescein intensity and side view (x−z plane) of the theoretical local intensity-interpreted Fl^{2-} concentration (expanded 300 times in the z direction) at various applied voltages.

dx.doi.org/10.1021/la500206b | *Langmuir* 2014, 30, 5337−5348

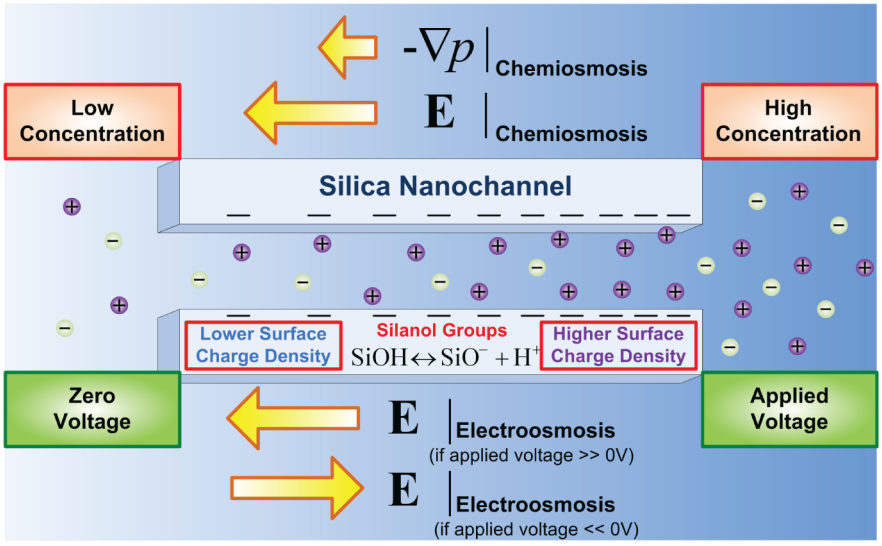

Figure 5. Schematic of the driving forces.

total fluxes are some (constant) multiple of the straight-channel simulation-predicted fluxes, namely, $q = Mq_{sim}$ and $i = Mi_{sim}$, and employ these equations to calculate ΔU. As simulations for all channel geometries have been performed for $\Delta u = 0$ V, we calculate M using this nanochannel voltage (using the data listed in the Supporting Information, Table SI 5.2) and assume that this M value also applies at other voltages. Using this method M is found to be very close to 6 (based independently on both flow rate and current), meaning that the total flow rate and current passing through the eight parallel nanochannels are almost equivalent to those that would pass through six straight nanochannels given the same potential difference. Full details are provided in the Supporting Information, SI 5.

4. RESULTS AND DISCUSSION

4.1. Rectangular Nanochannel. The concentration gradients generated at each applied voltage are observed from the fluorescence intensity in the experiments and are also numerically calculated. Figure 4a, b shows the intensity-interpreted Fl^{2-} oncentration in the straight nanochannel. The potentials in Figure 4a are the experimentally applied potentials, with the high salt concentration ports positively biased (ΔU). In the modeling (Figure 4b), the potentials inside the brackets are the potentials applied across the nanochannels (Δu) while the potentials outside the brackets are the potentials across the microchannels (ΔU) calculated via the electrokinetic circuit analysis. There is a high degree of correspondence between the experimental and simulations results, across the range of applied voltages. The closest quantitative correspondence between the results occurs at slightly different microchannel potentials (ΔU) however. These small differences are most likely due to two approximations used in the circuit analysis: (a) The multiplier M may show some dependence on the applied voltage (as detailed in Section 3.4, for practical reasons, M was calculated based on $\Delta u = 0$ results); and (b) the circuit analysis assumes that, when calculating the microchannel conductances, the salt concentrations are uniform and equal to the inlet values in each microchannel. In reality, ion transport through the nanochannels can affect these microchannel concentrations, altering the microchannel conductances (particularly the low concentration current conductance $\mathcal{L}_i'$), and this could produce an offset in the predicted ΔU values in line with those observed in Figure 4a, b.

The concentration profiles shown in Figure 4 are indicative of the bulk flow direction in the nanochannels. When the applied voltage is significantly positive ($\Delta U \gg 0$), the positively charged solution flows electroosmotically from the high TF concentration (right) microchannel to the low TF concentration (left) microchannel, bowing the concentration profile toward the low concentration end of the nanochannel. When $\Delta U \ll 0$, the direction of the flow is opposite, bowing the concentration profile the other way. The concentration profile is close to linear in the nanochannels when $\Delta U \approx 0$; however, there are some subtleties to these low potential profiles which are noteworthy: (a) The potential across the nanochannels is not zero ($\Delta u \approx -0.1$ V) when the concentration profile is closest to being linear; and (b) when the nanochannel voltage difference is zero, the concentration profile bows toward the low concentration end of the channel, suggesting that a bulk flow directed toward the low concentration end exists under these conditions ($\Delta u = 0$ and $\Delta U = 1.2$ V).

Both results can be attributed to chemiosmotic effects[42] that are present in the channel (driven by the concentration difference along the channel) that start to dominate electroosmotic effects when the applied potential is low. We now examine these chemiosmotic effects.

Within the double layer adjacent to the negatively charged silica surface, the potential is negative, creating an electric field that acts on the positively charged fluid to produce a force that is directed toward the solid. Concurrently, the pressure increases within the double layer, producing a counter-acting force on the fluid, directed away from the solid. Along a wall that has a uniform surface charge, surrounded by solute having a uniform (bulk) concentration, these pressure and electric forces cancel, and no fluid flow results.

In the present system, the solute concentration varies along the length of the channel. As the solute concentration increases, the double layer adjacent to the silica wall changes in two significant ways: (a) It becomes thinner due to the increased charge density in the fluid (the Debye length is inversely proportional to the square root of solute concentration); and (b) salt ions displace protons within the double layer, decreasing the number of uncharged silanol groups on the

dx.doi.org/10.1021/la500206b | Langmuir 2014, 30, 5337−5348

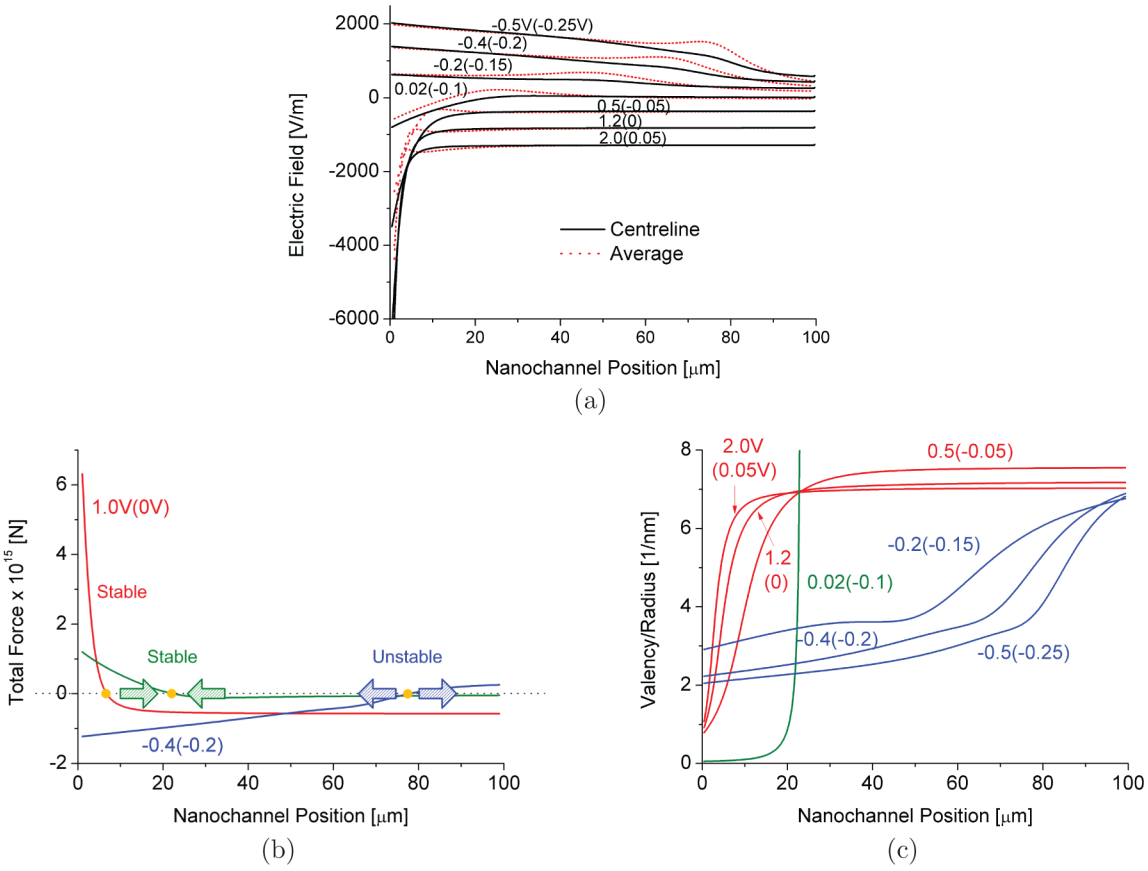

Figure 6. Rectangular nanochannel results: (a) Relationship between the axial electric field (in the x direction) and nanochannel position for various applied voltages. Black solid curves: the local electric field along the nanochannel centerline; red dot curves: the average electric field along the nanochannel. A positive field is directed toward the high concentration end of the nanochannel. (b) Trapping a negatively charged spherical particle in the rectangular nanochannel: The total force (hydrodynamic drag force + electric force) at the centerline of the nanochannel as a function of position and applied voltage is shown in frame (b). Orange dots indicate the zero total force (trap) locations. (c) Relationship between the valency/radius ratio, trap position, and applied voltage. Applied potentials are given (outside braces: ΔU; inside braces: Δu).

surface and increasing (in magnitude) the negative charge on the wall.

Both of these changes alter the pressure and potential fields near the walls and in so doing create tangential pressure and potential fields along the length of the channel (see Figure 5). These tangential fields can drive fluid flows toward either end of the channels via a process known as chemiosmosis.[42,43]

In the experiments conducted here at an applied nanochannel voltage of zero ($\Delta u \approx 0$), the chemiosmotic flow is directed toward the low concentration end of the channel, bowing the concentration profiles toward the low concentration microchannel as discussed above. The direction of this chemiosmotic flow is broadly consistent with the one-dimensional diffusioosmotic flow modeling performed by Ma and Keh.[42] Specifically, Ma and Keh show that, under similar conditions, the fluid flows toward the low concentration end of a channel when the nondimensional zeta potential magnitude is greater than approximately four. Ma and Keh's study did not employ the regulated surface charge model used here however and used a zero net current condition in their analysis (characteristic of diffusioosmotic flow) rather than a specified potential drop condition used here. Using additional simulations that employ an (artificially) varying surface charge within a two-dimensional channel containing a uniform (bulk) concentration solute, we found that the flow velocities produced are much smaller than for the full simulations, suggesting that effect (b) described above (increase in surface charge) is considerably less significant than effect (a) above (increase in solute concentration) for the system modeled here. Note that effect (a) is the more conventional description of chemiosmosis found in the literature.

The top view (x–y plane) of the experimental fluorescein intensity and side view (x–z plane) of the theoretical local intensity-interpreted FI^{2-} oncentration within a rectangular nanochannel is shown in Figure 4c. The concentration profile across the nanochannel depth direction (z direction), which is not available experimentally, is not uniform due to the overlapping double layers from the top and bottom walls of the nanochannel. The experimental results show that the ion concentrations are uniform across the channel width. Both observations are in line with the averaging assumptions employed in Section 3.1.

Figure 6a shows the electric field in the rectangular nanochannel as a function of applied voltage. The average and centerline electric fields are slightly different due to the presence of the (overlapping) double layers and channel end effects. The electric field becomes stronger as concentration (conductivity) decreases, qualitatively in line with species conservation along the channel (ignoring reaction effects) as described by eqs 9 and 10.

In modeling the trapping of proteins within their separation device, Inglis et al.[7] also modeled the formation of a chemical

dx.doi.org/10.1021/la500206b | Langmuir 2014, 30, 5337−5348

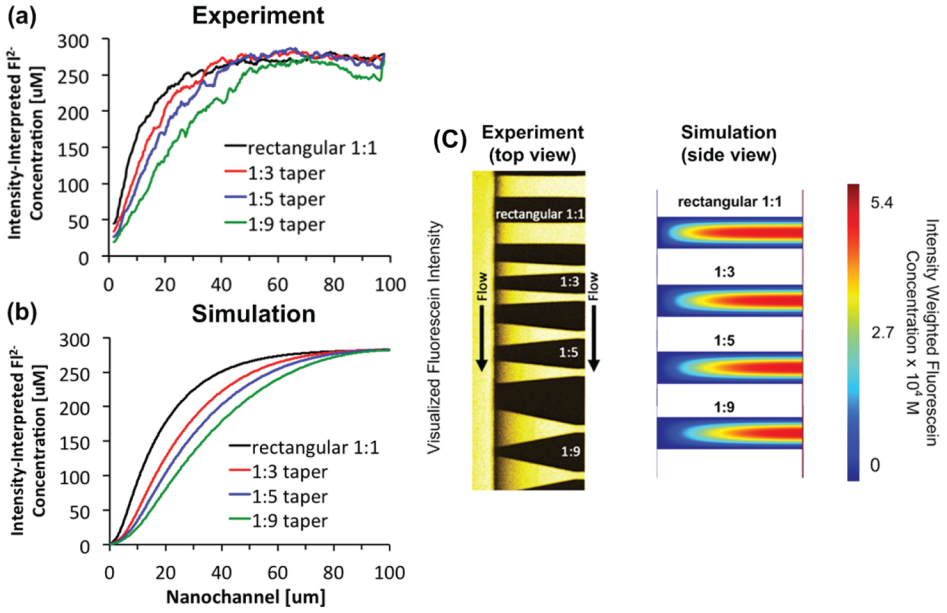

Figure 7. Concentrations within the tapered nanochannels: (a) experimental and (b) theoretical average intensity-interpreted Fl^{2-} concentration at ΔU = 1.2 V (Δu = 0 V) as a function of nanochannel taper. The tapered channels are widest at the low concentration (left) end of the nanochannel. Frame (c) shows the top view (x–y plane) of the experimental fluorescein intensity and side view (x–z plane) of the theoretical local intensity-interpreted Fl^{2-} concentration (expanded 300 times in the z direction) at ΔU = 1.2 V (Δu = 0 V) as a function of nanochannel taper.

gradient along the length of a nanochannel. While their model could reproduce observed concentration enhancements and qualitatively predict protein trapping behavior, several assumptions invalidate their concentration gradient model for more general (or design) use. First, a uniform nanochannel surface charge was employed, with multiple values used to ensure consistency between the different simulation and experimental measurements (−80 000 and −35 000 $e/\mu m^2$ were used in separate figures, as listed in their Supporting Information, Table 1). In contrast, the regulated surface charge model used here uses the same independently measured parameters for all simulations, reproducing the observed concentration gradients across a variety of applied voltages and nanochannel geometries (Section 4.3). Second, the previous model assumed that there were no electric potential drops within the microchannels, with the full potential drop over the device being applied across the nanochannels (4 V, as listed in their Supporting Information, Table 1). The circuit analysis conducted on the present system shows that the potential drops in the microchannels are comparable to those over the nanochannels, necessitating the use of the circuit model in quantitatively modeling this system.

4.2. Forces on Targeted Particles. An application for this controlled chemical gradient device is particle focusing and separation. Via electric field manipulation, trap locations and hence separation efficiency can be tuned. We discuss this behavior in the present thick double layer nanochannel using the example of a charged spherical particle.

The drag and electric forces that act on a particle depend on the local electric field and the velocity and are given by

$$\mathbf{F}_e = z_p e\mathbf{E} \quad \text{and} \quad \mathbf{F}_d = 6\pi\mu R_p \boldsymbol{\nu} \tag{19}$$

respectively, where z_p and R_p are the valency and hydrodynamic radius of the targeted particle, respectively. Particles are trapped at locations where the total force ($\mathbf{F}_d$ + $\mathbf{F}_e$) is zero. Hence, particles possessing the same (signed) valency (charge) to radius ratio (z_p/R_p) are trapped at the same location. Additionally, for a particle to be trapped, it must (a) have a charge of the same sign as the silica surface (i.e., negative) otherwise it would attach to the silica surface and (b) be at a "stable" trap location around which the total forces acting on the particle point toward (rather than away) the trap location.

To illustrate, Figure 6b shows the variation of total force on a negatively charged spherical particle at the centerline of the rectangular nanochannel at different applied electric voltages. Note that along the centerline of the channel, due to symmetry, the drag and electric force vectors are directed axially. The trapping behaviors observed at each applied electric potential can be classified into three categories: (i) the flow direction is the same as the diffusion direction; (ii) the solution is almost stagnant; (iii) the flow direction is opposite to the diffusion direction. For cases (i) and (ii), the gradients of the total force versus nanochannel position curves are negative (red and green curves) implying that any particle that is near the trap location is pushed toward the trap. Hence, cases (i) and (ii) are stable traps. Conversely, for case (iii), the gradient of the total force curve is positive (blue curve). Although the total force at the trap location is zero, if a particle were to deviate from this location, the total force on it would push if further away from the trap. Hence, case (iii) represents an unstable trap that would be ineffective for particle trapping. Note also for case (iii) that a negatively charged particle would not migrate into the nanochannel in the first place due to the overall force distribution.

The zero total force (trap) centerline locations for different levels of the valency/radius ratio are plotted in Figure 6c. For case (i) (red curves), a rapid increase of the electric field near the low TF concentration end of the nanochannel provides a separation zone for the particles (consistent with previous experimental observations in a similar system[7]). For case (ii), the green curve reveals that most of the particles are trapped at one specific location (~21 μm); however, due to the almost zero electric field and electroosmotic velocity, limited (or no) particles enter into the nanochannel. Hence, the focusing may

dx.doi.org/10.1021/la500206b | Langmuir 2014, 30, 5337−5348

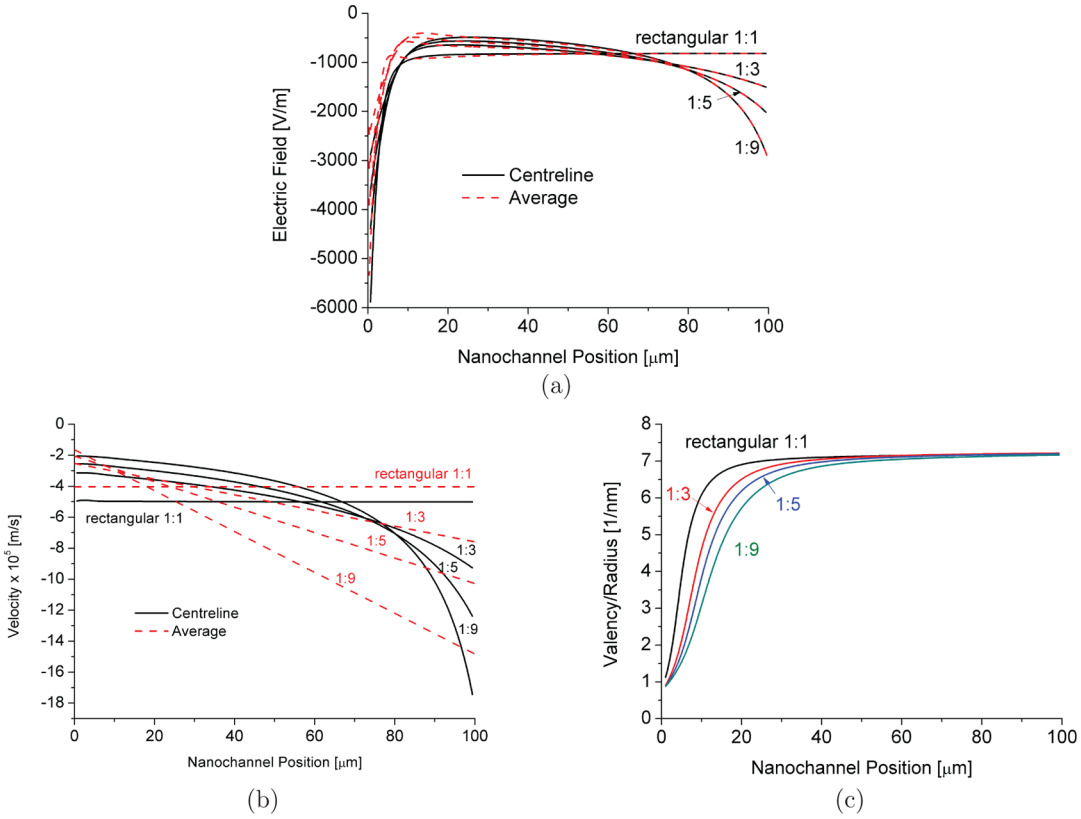

Figure 8. Tapered nanochannel results: The relationship between (a) the electric field and nanochannel position, (b) the velocity and nanochannel position, and (c) the valency/radius ratio and the trap location for a negatively charged spherical particle, at ΔU = 1.2 V (Δu = 0 V) as a function of nanochannel taper. In frames (a) and (b), black solid curves: the local value along the nanochannel centerline; red dot curves: the average value along the nanochannel.

be difficult to detect (or even not exist) despite the existence of the zero total force position in this case. For case (iii), the blue curves increase gradually from the low to high TF concentration ends; however, as discussed above, these traps are unstable and hence not suitable for particle focusing and separation.

4.3. Tapered Nanochannels. The influence of nanochannel shape on the solute concentration gradient is demonstrated in Figure 7. The simulation and experimental results are in good agreement, showing that our width averaged equations are able to capture the change in physical behavior as the geometry changes. For the displayed simulations where chemiosmosis is driving fluid flow from the high (right) concentration to low (left) concentration end of the nanochannel (Δu = 0 V), volume conservation dictates that the average fluid velocity at the low concentration end will be smaller than at the high concentration end. The principal effect of this is to reduce the magnitude of the advection term in the ion flux equations at the low concentration end of the nanochannel, thereby reducing the bowing of the concentration profiles observed in Figure 7a, b. For these low voltage conditions, the greater the degree of channel taper, the more linear the concentration profile.

The electric fields and velocity along the lengths of the tapered nanochannels are shown in Figure 8a, b. Again, for these simulations, Δu = 0 V, representing a chemiosmotically driven flow. The fields within the tapered channels have the same steep increase in magnitude near the low concentration end as observed for the straight channels but in contrast increase again from approximately 20 μm to a second maximum at the high concentration end. This increase, which occurs over the majority of the channel length and increases with taper amount, can be related back to the electrical Poisson eq 7. Noting that the total charge within the fluid contained within the channel is largely balanced by the wall charge along the majority of the channel length, this equation shows that the product of the average axial field and channel width is approximately uniform along the channel. Hence, as the channel width decreases, the field magnitude increases.

Figure 8c shows the net effect of the tapered channel field and drag forces on the centerline trap positions of a charged spherical particle, displayed as a function of the valency/radius ratio. At the same position, the particles trapped in the more highly tapered nanochannels have a smaller valency/radius ratio. For example, at 20 μm from the low concentration end, the valency/radius ratio is about 6.5 for the 1:5 tapered nanochannel but is less than 6 at the same location in the 1:9 tapered nanochannel. Significantly, the trap curves are less steep in the more highly tapered nanochannels, implying that particles of differing valency/radius ratio will be trapped at locations that are more widely spaced. Hence, the more tapered channels will show greater discrimination when used for particle separation. As discussed previously, the trap location of a particle is determined by the balance between the electrical and drag forces that act upon it. Hence, the greater separation sensitively that occurs in a tapered channel is not only due to the altered electrical field within the channel (as shown in Figure 8a) but also due the varying average velocity within the channel (as shown in Figure 8b).

dx.doi.org/10.1021/la500206b | *Langmuir* 2014, 30, 5337−5348

5. CONCLUSION

The variation of a fluorescein concentration gradient in response to an applied electric field in a nanofluidic device was investigated experimentally and via modeling. In the modeling, averaged governing equations based on cylindrical coordinates were adopted to simplify the three-dimensional system and allow accurate numerical solutions to be obtained. Also, a proton concentration governed charge regulated silica surface was used, with multiple reacting ionic species accounted for in the fluid. A high degree of correlation between the experimental and modeling results, in the absence of fitting parameters and for a variety of applied voltages and channel taper ratios, validates our approach. Using the simulations as an analysis tool, we have examined the performance of the channels to trap and separate particles. In the straight nanochannel, if the direction of flow is opposite to that of the salt gradient (that is, flows from the high to low concentration end), the electric field increases sharply at the low salt concentration end of the nanochannel, and the traps that form there are stable and can discriminate between particles of differing charge to size ratio. Trapping under these types of conditions has been observed previously.[7] If the net flow rate of fluid through the nanochannel is very low, the electric field may change direction near the low salt end of the nanochannel reducing the particle trap region to almost one specific location: Such a trap, although stable, would concentrate particles poorly and is not able to separate particles effectively. If the flow direction is the same as the salt gradient direction, all traps are unstable (and hence not physically realizable) as the net forces on any negatively charged particle are directed away from the trap location. In tapered nanochannels, the electric field increases at both ends of the channel, and due to this effect and the varying fluid velocity, channels with greater tapers are better able to achieve particle separation.

■ ASSOCIATED CONTENT

Ⓢ Supporting Information

Averaging identities, averaged equations, chemical reactions, nanochannel boundary conditions, and circuit analysis. This material is available free of charge via the Internet at http://pubs.acs.org.

■ AUTHOR INFORMATION

Corresponding Author

*Phone: +61 3 8344 6421; fax: +61 3 8344 4153; e-mail: daltonh@unimelb.edu.au.

Notes

The authors declare no competing financial interest.

■ ACKNOWLEDGMENTS

The authors are grateful to Mirek Macka (University of Tasmania) for his suggestion to buffer fluorescein with Tris. Thermal oxidation was performed at the University of New South Wales; node and photomasks were made at the Optofab node of the Australian National Fabrication Facility, established under NCRIS.

■ REFERENCES

(1) Dekker, L.; Segal, A. Signal Transduction - Signals to Move Cells. *Science* **2000**, *287*, 982−985.

(2) Song, H.; Poo, M. Signal Transduction Underlying Growth Cone Guidance by Diffusible Factors. *Curr. Opin. Neurobiol.* **1999**, *9*, 355−363.

(3) Aizenberg, J.; Black, A.; Whitesides, G. Control of Crystal Nucleation by Patterned Self-Assembled Monolayers. *Nature* **1999**, *398*, 495−498.

(4) Kelly, K. C.; Miller, S. A.; Timperman, A. T. Investigation of Zone Migration in a Current Rectifying Nanofluidic/Microfluidic Analyte Concentrator. *Anal. Chem.* **2009**, *81*, 732−738.

(5) Quist, J.; Janssen, K. G. H.; Vulto, P.; Hankemeier, T.; van der Linden, H. J. Single-Electrolyte Isotachophoresis Using a Nanochannel-Induced Depletion Zone. *Anal. Chem.* **2011**, *83*, 7910−7915.

(6) Basak, S.; Velayudhan, A.; Kohlmann, K.; Ladisch, M. Electrochromatographic Separation of Proteins. *J. Chromatogr. A* **1995**, *707*, 69−76.

(7) Inglis, D. W.; Goldys, E. M.; Calander, N. P. Simultaneous Concentration and Separation of Proteins in a Nanochannel. *Angew. Chem., Int. Ed.* **2011**, *50*, 7546−7550.

(8) Wang, Y.-C.; Han, J. Pre-binding Dynamic Range and Sensitivity Enhancement for Immuno-Sensors Using Nanofluidic Preconcentrator. *Lab Chip* **2008**, *8*, 392−394.

(9) Sustarich, J. M.; Storey, B. D.; Pennathur, S. Field-Amplified Sample Stacking and Focusing in Nanofluidic Channels. *Phys. Fluids* **2010**, *22*, 112003.

(10) Kwak, R.; Kim, S. J.; Han, J. Continuous-Flow Biomolecule and Cell Concentrator by Ion Concentration Polarization. *Anal. Chem.* **2011**, *83*, 7348−7355.

(11) Greenlee, R.; Ivory, C. Protein Focusing in a Conductivity Gradient. *Biotechnol. Prog.* **1998**, *14*, 300−309.

(12) Abhyankar, V.; Lokuta, M.; Huttenlocher, A.; Beebe, D. Characterization of a Membrane-Based Gradient Generator for Use in Cell-Signaling Studies. *Lab Chip* **2006**, *6*, 389−393.

(13) de Jong, J.; Verheijden, P. W.; Lammertink, R. G. H.; Wessling, M. Generation of Local Concentration Gradients by Gas-Liquid Contacting. *Anal. Chem.* **2008**, *80*, 3190−3197.

(14) Irimia, D.; Geba, D.; Toner, M. Universal Microfluidic Gradient Generator. *Anal. Chem.* **2006**, *78*, 3472−3477.

(15) Tehranirokh, M.; Kouzani, A. Z.; Francis, P. S.; Kanwar, J. R. Generating Different Profiles of Gradient Concentrations Inside a Gel-Filled Chamber: Design and Simulation. *Microsyst. Technol.* **2013**, *19*, 623−628.

(16) Jeon, N.; Dertinger, S.; Chiu, D.; Choi, I.; Stroock, A.; Whitesides, G. Generation of Solution and Surface Gradients Using Microfluidic Systems. *Langmuir* **2000**, *16*, 8311−8316.

(17) Zangle, T. A.; Mani, A.; Santiago, J. G. On the Propagation of Concentration Polarization from Microchannel-Nanochannel Interfaces Part II: Numerical and Experimental Study. *Langmuir* **2009**, *25*, 3909−3916.

(18) Zangle, T. A.; Mani, A.; Santiago, J. G. Effects of Constant Voltage on Time Evolution of Propagating Concentration Polarization. *Anal. Chem.* **2010**, *82*, 3114−3117.

(19) Mani, A.; Zangle, T. A.; Santiago, J. G. On the Propagation of Concentration Polarization from Microchannel-Nanochannel Interfaces Part I: Analytical Model and Characteristic Analysis. *Langmuir* **2009**, *25*, 3898−3908.

(20) Petsev, D.; Lopez, G.; Ivory, C.; Sibbett, S. Microchannel Protein Separation by Electric Field Gradient Focusing. *Lab Chip* **2005**, *5*, 587−597.

(21) Ghosal, S.; Horek, J. Mathematical Model Describing Gradient Focusing Methods for Trace Analytes. *Anal. Chem.* **2005**, *77*, 5380−5384.

(22) Keh, H.; Wu, J. Electrokinetic Flow in Fine Capillaries Caused by Gradients of Electrolyte Concentration. *Langmuir* **2001**, *17*, 4216−4222.

(23) Wu, J.; Keh, H. Diffusioosmosis and Electroosmosis in a Capillary Slit with Surface Charge Layers. *Colloids Surf., A* **2003**, *212*, 27−42.

(24) Ma, H.; Keh, H. Diffusioosmosis of Electrolyte Solutions in a Fine Capillary Slit. *J. Colloid Interface Sci.* **2006**, *298*, 476−486.

(25) Andersen, M. B.; Bruus, H.; Bardhan, J. P.; Pennathur, S. Streaming Current and Wall Dissolution over 48 h in Silica Nanochannels. *J. Colloid Interface Sci.* **2011**, *360*, 262−271.
(26) Behrens, S.; Grier, D. The Charge of Glass and Silica Surfaces. *J. Chem. Phys.* **2001**, *115*, 6716−6721.
(27) Lorenz, C. D.; Crozier, P. S.; Anderson, J. A.; Travesset, A. Molecular Dynamics of Ionic Transport and Electrokinetic Effects in Realistic Silica Channels. *J. Phys. Chem. C* **2008**, *112*, 10222−10232.
(28) Tseng, S.; Tai, Y.-H.; Hsu, J.-P. Electrokinetic flow in a pH-Regulated, Cylindrical Nanochannel Containing Multiple Ionic Species. *Microfluid. Nanofluid.* **2013**, *15*, 847−857.
(29) Yeh, L.-H.; Zhang, M.; Qian, S. Ion Transport in a pH-Regulated Nanopore. *Anal. Chem.* **2013**, *85*, 7527−7534.
(30) Cervera, J.; Schiedt, B.; Neumann, R.; Mafe, S.; Ramirez, P. Ionic Conduction, Rectification, and Selectivity in Single Conical Nanopores. *J. Chem. Phys.* **2006**, *124*, 104706.
(31) Diehl, H.; Markuszewski, R. Studies on Fluorescein 0.7. Fluorescence of Fluorescein as a Function of pH. *Talanta* **1989**, *36*, 416−418.
(32) Persat, A.; Chambers, R. D.; Santiago, J. G. Basic Principles of Electrolyte Chemistry for Microfluidic Electrokinetics. Part I: Acid-Base Equilibria and pH Buffers. *Lab Chip* **2009**, *9*, 2437−2453.
(33) Harvie, D. J. E. An Implicit Finite Volume Method for Arbitrary Transport Equations. *ANZIAM J.* **2012**, *52*, C1126−C1145.
(34) Biscombe, C. J. C.; Davidson, M. R.; Harvie, D. J. E. Electrokinetic Flow in Parallel Channels: Circuit Modelling for Microfluidics and Membranes. *Colloids Surf., A* **2014**, *440*, 63−73.
(35) Berry, J. D.; Davidson, M. R.; Harvie, D. J. E. Electroviscous Flow Through Nanofluidic Junctions. *Appl. Math. Model.* **2014**, in press.
(36) Mason, L. R.; Ciceri, D.; Harvie, D. J. E.; Perera, J. M.; Stevens, G. W. Modelling of Interfacial Mass Transfer in Microfluidic Solvent Extraction: Part I. Heterogenous Transport. *Microfluid. Nanofluid.* **2013**, *14*, 197−212.
(37) Ciceri, D.; Mason, L. R.; Harvie, D. J. E.; Perera, J. M.; Stevens, G. W. Modelling of Interfacial Mass Transfer in Microfluidic Solvent Extraction: Part II. Heterogeneous Transport with Chemical Reaction. *Microfluid. Nanofluid.* **2013**, *14*, 213−224.
(38) Harvie, D. J. E. arb. http://people.eng.unimelb.edu.au/daltonh/downloads/arb/code/latest/examples/electrokinetic_channel_flow/, accessed on 10th April 2014.
(39) Geuzaine, C.; Remacle, J.-F. Gmsh: A 3-D Finite Element Mesh Generator with Built-in Pre- and Post-processing Facilities. *Int. J. Numer. Methods Eng.* **2009**, *79*, 1309−1331.
(40) Biscombe, C. J. C.; Davidson, M. R.; Harvie, D. J. E. Electrokinetic Flow in Connected Channels: A Comparison of Two Circuit Models. *Microfluid. Nanofluid.* **2012**, *13*, 481−490.
(41) Harvie, D. J. E.; Biscombe, C. J. C.; Davidson, M. R. Microfluidic Circuit Analysis I: Ion Current Relationships for Thin Slits and Pipes. *J. Colloid Interface Sci.* **2012**, *365*, 1−15.
(42) Ma, H. C.; Keh, H. J. Diffusioosmosis of Electrolyte Solutions in a Fine Capillary Slit. *J. Colloid Interface Sci.* **2006**, *298*, 476−486.
(43) Liu, K.-L.; Hsu, J.-P.; Tseng, S. Capillary Osmosis in a Charged Nanopore Connecting Two Large Reservoirs. *Langmuir* **2013**, *29*, 9598−9603.